eprints@whiterose.ac.uk
https://eprints.whiterose.ac.uk/

Single Source Three Dimensional Capture of Full Field Plate Vibrations

A.D. Shaw   S.A. Neild   D.J. Wagg   P.M. Weaver

February 2011

Abstract

Measurement of the vibrations of plates can offer significant challenges to the experimentalist, particularly when the plates are lightweight, exhibit large amplitude deflections, nonlinear responses or are initially curved. The use of accelerometers adds masses which can change the dynamics of lightweight plates. Large amplitude oscillations and initial curvatures cause complications when using a laser vibrometer, as they make it difficult to get consistent reflections back to the receiver. Furthermore, large or nonlinear oscillations challenge inherent assumptions on which the vibrometer's algorithms depend. A high speed video camera avoids these issues, but makes it hard to extract numerical data.

This paper describes a method that extends the capabilities of a high speed video camera by using a mirror, allowing post-processing software to stereoscopically resolve an array of points on the plate surface to 3D coordinates, capturing the complete shape and position of the plate throughout vibration. This method avoids all the problems mentioned above and gives very clear insight into plate vibration.

Some example results of this method are presented, using thermally bistable carbon laminate plates filmed at a 1000 frames per second. These plates pose the challenges described, and also exhibit an unusual oscillatory motion where the plates 'snap' between two statically stable states. The method is shown to provide clear insight into the rich dynamics of these plates.

1   Introduction

There are numerous methods for measuring vibration of systems that may be broadly separated into 'contact' and 'non-contact' techniques. Contact methods involve physi-

cally attaching transducers (usually accelerometers) to the structure that is being anal-ysed, and are well-proven in many contexts [6]. However, when the structure has low mass, such as a thin plate, the additional mass of the attached sensors has an undesirable influence on the system being analysed. Furthermore, practical limits on the number of sensors deployed mean that in general they do not resolve a 'full field' deflection shape.

Non-contact methods require little or no attachments to the structure under test, and therefore they avoid the problem of unwanted mass. The predominant example of a non-contact method is the use of the Laser Doppler Vibrometer (LDV), or for full-field measurements, the Scanning Laser Doppler Vibrometer (SLDV). The LDV works by directing laser light at a target on the structure under test, which is reflected back to a receiver that measures the Doppler-shifted wavelength with an interferometer, which is then used to calculate the velocity of the target. A number of instantaneous velocities are measured over a period of time to deduce the resulting vibration. An SLDV extends this by using a controller to perform the test on an array of pre-selected targets, to create a full field measurement. This method is successfully used on a widespread basis [6].

However, there are certain situations where the use of the SLDV proves limiting. One example is the measurement of curved plates; the curvature can mean that light is reflected away from the receiver, leading to poor resolution of the signal. Furthermore, when oscillations become large, there may be significant motion that is in the plane normal to the laser beam. This poses two problems; the first that the vibrometer may not capture the true amplitude of vibration, and the second that the laser target is moving relative to the physical surface of the plate.

A second problem with SLDV tests occurs when complex and nonlinear responses are encountered. The SLDV does not measure each point simultaneously; each point is measured in turn, and then the measured signals are combined to provide a view of the overall deflection motions (an exception to this is the Continuous-Scan LDV as described by Stanbridge *et al.* [14]). The algorithms that perform these calculations are generally proprietary and not typically available to the researcher; therefore it is unknown whether they are valid in the case of non-linear vibrations, particularly if chaotic motions are encountered. Furthermore, because the LDV is a velocity measuring device, there is no true check of the shape of the plate at any given point; the mean point of oscillation is assumed to be the static shape, when this is not necessarily true for nonlinear oscillation.

Another non-contact strategy that can be used is high-speed video. However, on its own this method will only provide a qualitative view of the vibration behaviour.

There is a wide body on stereoscopic imaging systems, that make use of multiple images of a single scene to provide detailed 3D measurements [7, 11]. One approach to stereoscopic imaging is to use mirrors to generate multiple views, saving the com-plexity and cost of additional cameras. This approach also eliminates the need to syn-chronize cameras, although it is penalised by a reduction in the field of view, due to multiple perspectives being served by one image. Lin et al. [9] and Ma *et al.* [10] have used multiple mirror systems for the capture of facial motion for the purpose of com-puter animation. Putze *et al.* [13] describes multiple mirror systems combined with a high speed video cameras, and shows that they can achieve comparable accuracy to multi-camera systems. Duvieubourg *et al.* describe a system using a system movable
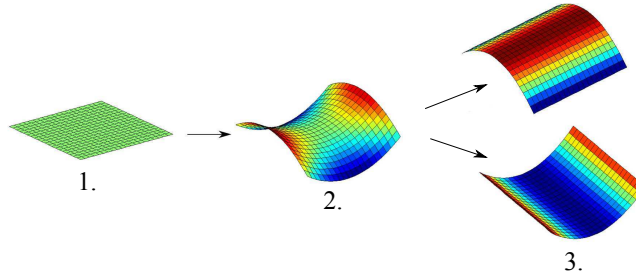
Figure 1: Process of bistable plate manufacture. (1) A flat laminate of directional plies with asymmetric stacking sequence is cured at elevated temperature in an autoclave. (2) On initial cooling the plate distorts into a saddle shape, due to contraction that is asymmetric through its thickness. (3) On further cooling, as curvature increases, the saddle becomes unstable, and the plate adopts one of two possible stable configurations, which it can 'snap' between

mirrors to provide an orientable view of a scene [15]. Pankow *et al.* used a multi-mirror system to measure deformation of thin plates in response to shocks [12].

This paper outlines a method that extends the use of a high speed digital video camera with just a single mirror. The technique allows the 3D locations of points over the surface of a plate to be recorded in each frame of the video, thereby measuring the full field motion of the plate. It therefore avoids unwanted mass, and makes no assumptions about the nature of the motion being measured. Furthermore, it directly captures shape information. The paper therefore extends the use of stereoscopic vision to gain new insights in the fields of plate dynamics.

To demonstrate the method, the case of a bistable curved laminated plate is considered, which will be described in section 2. Section 3 describes the image capture and data processing method, and Section 5 presents some example vibration responses for bistable plates. Conclusions are drawn in Section 6.

2   Case Study - Curved Bistable Plates

The experiment for which the method was developed was an investigation into the vibration mode shapes of bistable carbon composite laminated plates. These are plates made from asymmetric laminates of carbon/epoxy plies which distort on cooling from the cure temperature due to the directional thermal expansion coefficients of the plies [2]. At room temperature they 'snap' between two stable configurations [2]. Figure 1 briefly shows how these plates are formed. Such plates have possible applications in morphing structures. Their use in such structures is being investigated in order to exploit the property of multiple stable states [3] [4].

The dynamics of these plates are characterised by a double well potential, where the two wells represent the two stable configurations of the plate. Small oscillations can occur within each well, but larger oscillations can encompass both potential wells,
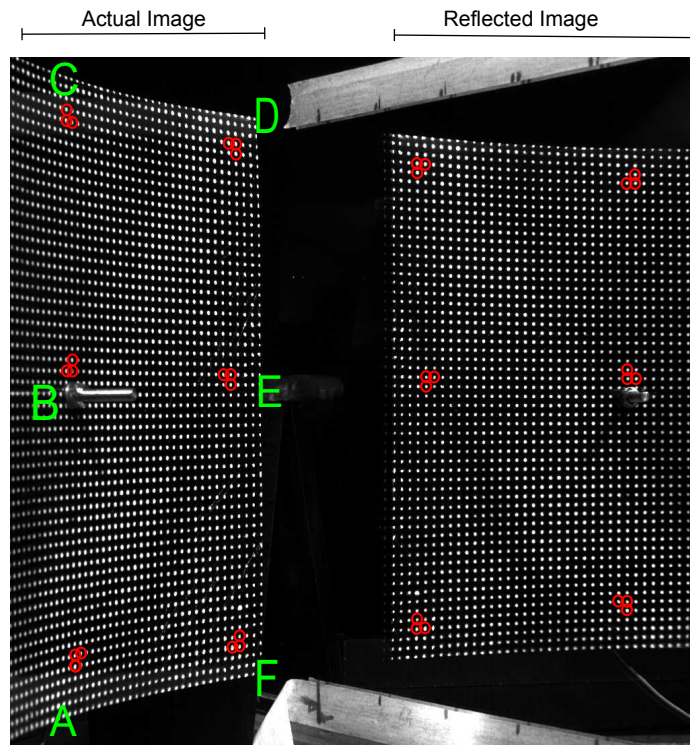
Figure 2: Typical image for processing. Points A-F are reference locations on the surface of the plate, circles show manually selected points for calibration. Note that in this case, only half the plate has been filmed to make best use of the camera resolution; the other half can be inferred in the typical case of symmetric or antisymmetric motion

in a 'snapping' motion. These larger oscillations can show chaotic motion [1].

These plates pose substantial difficulties to conventional vibration measurement systems, because of the radical shape changes they can undergo during oscillation. They also pose complications for high speed image capture, due to the naturally dark and featureless surface of their material. Furthermore, it had been found during a previous experiment that completely painting the plates (e.g. with a speckle pattern) had a significant effect on their properties, which are known to vary significantly even in response to ambient humidity [5]. The use of an array of dots as motion targets was chosen as a compromise solution to these problems.
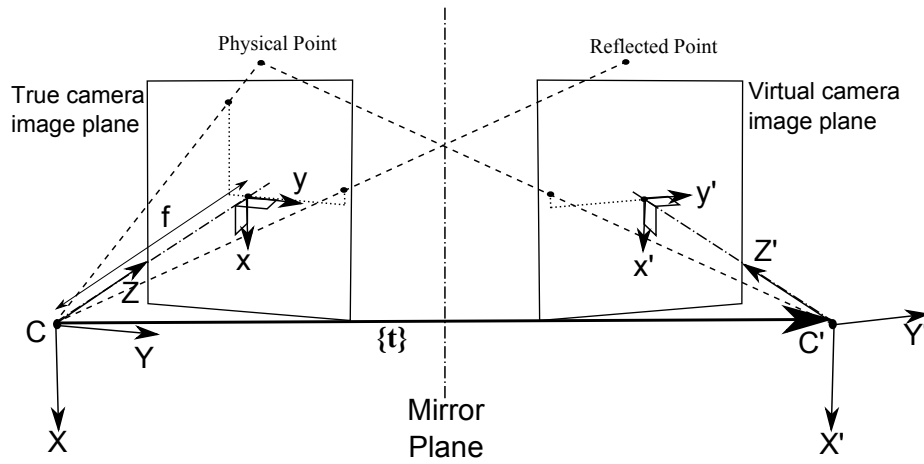
Figure 3: Diagram illustrating the geometric principle of using a mirror for stereoscopic resolution. The true camera's focal point at C is the origin of the 'True camera' coordinate system. The true camera's projection of the reflected point is a simple reflected transformation of the projection of the physical point in a 'Virtual camera' system with origin at point C'. Hence the reflection can be used to construct a stereoscopic system, as if a second camera existed at C'. $\{t\}$ is the translation vector between the origins of the two coordinate systems

3 Description of Method

3.1 Overview

A high speed camera is used to record the motion of points on the structure, along with their reflections in an angled mirror which allows post-processing software to resolve 3D locations of points painted on the plate surface. The camera used for the case study was a Photron Fastcam SA1, running at 1000 frames per second.

Figure 2 shows a typical single frame captured by the camera during the case study experiment. The image processing routine traces the 3D location of each dot by using the dot's reflection to perform a triangulation. To make best use of the camera resolution, only half of the plate was filmed for the case study; line AC in Figure 2 is a centreline of the plate. The other half of the plate could be inferred by the symmetry or antisymmetry of the observed deflections.

The stages of this experimental method are:

1. Use our Matlab-based software to calibrate its position with regard to the mirror, as detailed in Section 3.2.

2. Extract 2D image coordinates of points from the images taken, as described in section 3.3.

3. Establish correspondence between true image points with reflected image points,

and triangulate the resulting 3D location, as detailed in Section 3.4 and Section 3.5.

4. Final data transformation and reduction, as described in Section 3.6.

These stages are described in the subsequent sections.

3.2 Calibration

Figure 3 shows the geometry of the method. A simple forward-projection pinhole model is used to represent the camera, and its virtual equivalent. For simplicity we assume that sensor coordinates are unskewed and already transformed into the system shown as x, y, x' and y' in Figure 3. We also assume that the virtual camera is identical to the true camera, an assumption that implies that the mirror has no effect on the apparent internal properties of the virtual camera, and therefore both cameras have the same focal length f.

The true camera's focal point C is the origin of the 'true' coordinate system as shown in Figure 3, and the virtual camera's focal point C' is the origin of the 'virtual' coordinate system. Coordinates in the true camera system can be transformed to the virtual coordinate system by means of a simple rotation and transformation; mathematically if P and P' represent the same physical point in the true and virtual coordinate systems respectively we may write:

$$\{P'\} = [R]\{P\} + \{t\} \tag{1}$$

where $\{P\} = \{X,Y,Z\}^T$, $\{P'\} = \{X',Y',Z'\}^T$, the translation vector $\{t\} = \{t_1,t_2,t_3\}^T$ and $[R]$ is the 3D rotation matrix given as:

$$[R] = \begin{bmatrix} R_{11} & R_{12} & R_{13} \\ R_{21} & R_{22} & R_{23} \\ R_{31} & R_{32} & R_{33} \end{bmatrix}$$

The task of calibration is therefore to establish $[R]$ and $\{t\}$. Note that $[R]$ allows any 3D rotation, and can therefore compensate for any misalignment of the image verticals with the mirror plane.

The calibration process used is a simplified form of the bundled adjustment procedure as described by Sutton *et al.* [11], solving for just the rotation and translation between camera systems. Firstly, using interactive routines from Matlab's image processing toolbox [8], the user manually selects a number of corresponding pairs of points from the true and reflected image, as shown in Figure 2. These are grouped in threes so that the local plane can be resolved, which is used in Section 3.4.3. The routines locate the centroidal position of each selected point.

The calibration procedure then minimises a least squares metric based on the distance in each image plane between the sensor coordinates for each point, and the true projections of the 3D point as implied by the given parameters:

$$E = \sum_{n=1}^{N} (x_n - \hat{x}_n(\beta))^2 + (y_n - \hat{y}_n(\beta))^2 + (x'_n - \hat{x}'_n(\beta))^2 + (y'_n - \hat{y}'_n(\beta))^2 \tag{2}$$

where x_n, y_n and x'_n, y'_n are the sensor coordinates in the true and virtual image planes respectively, $\hat{x}_n$, $\hat{y}_n$, $\hat{x}'_n$ and $\hat{y}'_n$ are the image plane coordinates projected from the calculated 3D points, and β is a vector of the parameters to be tuned. The components of β are given by:

$$\beta = \{n_1, n_2, n_3, t_1, t_2, t_3\}^T \tag{3}$$

where n_1, n_2 and n_3 are components of a vector forming the minimal parametrisation of $[R]$, where the direction of the vector defines the axis of rotation, and the magnitude of its angle in radians [11], and t_1, t_2 and t_3 are components of the translation vector $\{t\}$. Hence to calculate $\hat{x}_n(\beta)$, the procedure calculates the 3D position of the point P_n implied by the true and reflected points and current parameters, using the method described in Section 3.5, and then evaluates:

$$\hat{x}_n = f\frac{X_n}{Z_n} \quad , \quad \hat{y}_n = f\frac{Y_n}{Z_n} \tag{4}$$

which can be derived graphically from Figure 3. For $\hat{x}'_n$ and $\hat{y}'_n$, the 3D coordinates must be transformed into the virtual coordinate system using Equation 1 and the calculation is then similar to Equation 4.

E is minimised using a Levenberg-Marquardt solver to perform the nonlinear optimisation, where the initial values may be estimated using standard geometry. The solver was as implemented within the Matlab function `lsqnonlin` [8]. Finally, to provide useful dimensional units to the returned coordinates, a scaling factor for the system is calculated based on known distances between the physical points used for calibration. Note that in this simple model, focal length f is effectively an arbitrary scaling factor, which could vary infinitely if $\{t\}$ varied accordingly, so it is held constant during optimisation.

3.3 Extraction of 2D Positional Data

Matlab's image processing toolbox routines [8] were used to interactively mask the true image region and the reflected region, to create separate images. The images were then reduced to binary images whereby each pixel is set to either 1 or 0 according to whether its brightness exceeds a certain threshold, using Matlab function `im2bw`. Each dot is therefore represented as an interconnected region of ones in the grid of pixel values. Matlab's function `bwconncomp` is then used to locate these regions, and the function `regionprops` is used to automatically calculate their centroids. In this manner both the true and reflected images are reduced to simple lists of 2D points on the image plane. The virtual image points are reflected about the central vertical axis, so that the geometry of Figure 3 may be realised.

3.4 Correspondence

It was found that small flaws in the material surface could occasionally cause spurious reflections that caused 'noise points' in either the true or reflected images. Furthermore, near the edges a true point's reflection may be outside the image boundary, or vice versa. Given these circumstances, multiple correspondence strategies were chosen to provide the most robust matching possible. These were:

7

- Epipolar constraint

- Ordering

- Surface planarity

- Uniqueness

These are detailed in the following subsections.

3.4.1 Epipolar constraint

This constraint is discussed widely in literature on stereoscopic imaging [7, 11]. As can be seen in Figure 3, the physical point, its projections, both camera origins and the translation vector between them must all lie in a common plane, known as the epipolar plane. Therefore the epipolar planes for all sensor points are resolved using standard vector geometry, and any pairings of true and virtual points where the angles of plane differ outside a certain error tolerance (in this experiment 0.03°) are rejected.

3.4.2 Ordering constraint

The subject of the measurement is a single continuous surface, so therefore it is possible to eliminate many candidate matches based on an ordering constraint as described by Faugeras [7]. The geometrical basis of this constraint is shown in Figure 4. The projected distance of all points onto the direction of the stereoscopic translation vector $\{t\}$ is calculated using the dot product. This is then used to sort all true and mirror points. Hence whenever a correspondence is found with sensor locations $\{p\}$ and $\{p'\}$ in true and virtual image planes respectively, the algorithm finds all true and reflected points within tolerance of their epipolar planes, and eliminates any correspondences where the true point occurs before $\{p\}$ and the mirror point after $\{p'\}$ or vice versa.

3.4.3 Surface Planarity

This test uses the fact that the test subject is a smooth surface, effectively limiting local surface curvature. Figure 5 illustrates the geometry of the test. A candidate pair of points has its implied 3D position calculated as described in Section 3.5. The algorithm then searches for 3 other previously calculated and confirmed points within a 3D zone near this point. It also ensures that these points are not close to being aligned with each another and are not too close to one another, so that they offer good resolution of the local surface plane orientation. If this search is successful the algorithm calculates the angle ε as shown in Figure 5 using vector geometry. If this angle is greater than a specified limit ε_{max}, implying that the point does not appear to lie near to the local surface plane, the candidate pairing is rejected. For many candidate pairings, this test will initially fail to find nearby points with which to perform the comparison. These points must therefore wait till later passes through the data occur, as described in Section 3.4.5, to be confirmed or rejected by this test.

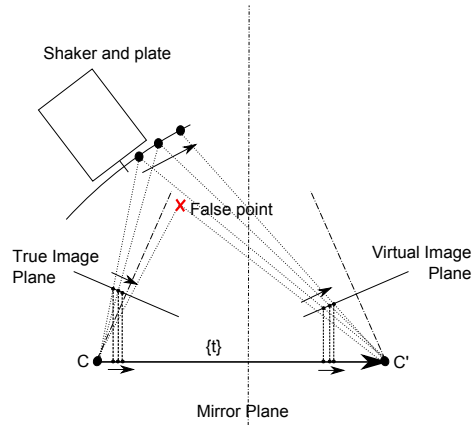The 3D zone used in this case was a cubic zone of side 32mm, and ε_{max} was set to 3°.

Figure 4: Diagram showing the principle of the ordering constraint. A collection of points within a single epipolar plane must preserve their order in the direction of the translation vector $\{t\}$ in both images. A candidate pairing which does not respect this ordering will apparently lie in front or behind the surface of other dots, and therefore be false
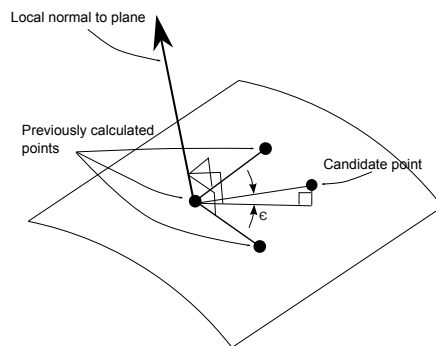

Figure 5: Method used to find ε to test for point validity. A vector is calculated between the candidate point and a previously calculated point. The angle ε between this vector and the local surface plane is then calculated, and compared to a threshold. The local surface is defined by its normal vector, which is found with the use of two other previously calculated points

9

3.4.4 Uniqueness constraint

If, for a given true image point, there are multiple pairings with virtual images points that pass all the above constraints, none of these pairings are confirmed as true correspondences. Similarly, if multiple true image points pass the above tests when paired with a single mirror image point, none of these pairings are confirmed. This is a conservative strategy to handle the case where noise points exist so near to an actual point that the resulting 3D point calculation can still pass other tests. This can cause a true correspondence to be rejected along with the 'noise' pairing, but with the large numbers of points present in the grid, the numbers of points lost in this way is insignificant.

3.4.5 Overall correspondence algorithm

In the experiment shown there are approximately 2000 visible points in the grid, appearing in each of the true and mirror images, leading to around 4 million candidate pairings. The epipolar constraint is used to filter this list, and typically leaves approximately 20000 candidate pairings. The calibration points are then added to the list of confirmed 3D points, and used to reject further pairings based on the ordering constraint. Then for all remaining candidate pairings:

- If possible, the planarity test is calculated, and candidate pairs that fail are rejected.

- Any candidate pairs that have passed the planarity test and pass the uniqueness constraint are added to the list of confirmed points, and used to perform further filtering with the ordering constraint.

- This process is repeated for all points until no more pairings are confirmed or rejected.

3.5   Skew Triangulation of 3D Points

The 3D triangulation method is a simple implementation 'skew triangulation' method, as described in much of the literature [7, 11]. Referring to Figure 3, the relationship between a point at $\{X,Y,Z\}^T$ in the true camera image system, and its image plane coordinates $\{x,y\}^T$ may be written

$$
\begin{aligned}
fX + 0Y - xZ = 0 \\
0X + fY - yZ = 0
\end{aligned}
$$
(5)

The same relationship may be written for the virtual camera system and image plane:

$$
\begin{aligned}
fX' + 0Y' - x'Z' = 0 \\
0X' + fY' - y'Z' = 0
\end{aligned}
$$
(6)

10

Substituting Equation (1) into (6) gives:

$$(fR_{11} - x'R_{31})X + (fR_{12} - x'R_{32})Y + (fR_{13} - x'R_{33})Z = -ft_1 + x't_3$$
$$(fR_{21} - y'R_{31})X + (fR_{22} - y'R_{32})Y + (fR_{23} - y'R_{33})Z = -ft_2 + y't_3 \tag{7}$$

Equations (5) and (7) form an overconstrained set of equations that may be written in matrix form as:

$$[M]\{P\} = \begin{bmatrix} M_{11} & M_{12} & M_{13} \\ M_{21} & M_{22} & M_{23} \\ M_{31} & M_{32} & M_{33} \\ M_{41} & M_{42} & M_{43} \end{bmatrix} \begin{Bmatrix} X \\ Y \\ Z \end{Bmatrix} = \begin{Bmatrix} 0 \\ 0 \\ -ft_1 + x't_3 \\ -ft_2 + y't_3 \end{Bmatrix} = \{r\} \tag{8}$$

This is solved using the generalised inverse as follows:

$$\{P\} = \left([M]^T [M]\right)^{-1} [M]^T \{r\} \tag{9}$$

Therefore Equation (9) is used to calculate the 3D point $\{P\} = \{X, Y, Z\}^T$ given sensor coordinate values for $\{x, y\}^T$ and $\{x', y'\}^T$, and the stereoscopic rotation matrix and translation vector.

3.6   Data Transformation and Reduction

Generally it will be required to perform a coordinate transformations to find more useful coordinate system, e.g so that x and y are the approximate plane of the plate and z is normal to this plane. Then, it will typically be required to calculate 3D displacements, by taking a single image of the plate at rest and subtracting these coordinates from those for each individual frame of the plate in motion.

The Matlab surface fitting toolbox is then used to fit a 5th order polynomial surface to the data [8]. Figure 6 shows two snapshots at opposite peaks of the vertical displacement field of a curved plate in a given mode of vibration, including both the actual data points calculated and the smoothed surface. As seen in Figure 6, this fitted surface lies within the noise level of the data in all parts of the plate, and provides much clearer views of mode shapes than a 'cloud' of separate dots can provide.

4   Error Analysis

As a means of confirming the accuracy of the method, an error estimation was carried out using the geometry shown in figure 7, where P is a point calculated by the routine with coordinates (X, Y, Z) in the true camera system, (x, y) are its associated sensor coordinates in the true camera system and $(\hat{x}, \hat{y})$ is the calculated projection onto the true image plane using the calibrated model parameters, where:

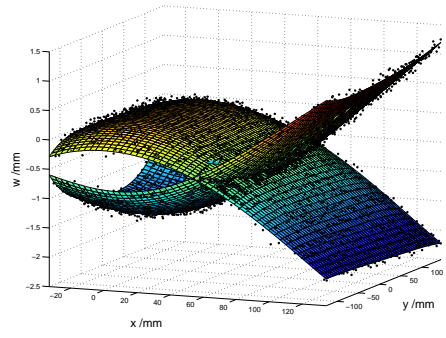$$\hat{x} = X\frac{f}{Z} \quad , \quad \hat{y} = Y\frac{f}{Z} \tag{10}$$

11

Figure 6: Typical vertical displacement plot at peaks of oscillations, showing quality of polynomial fit
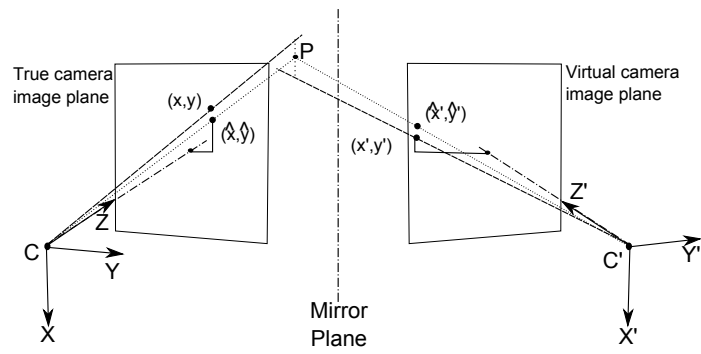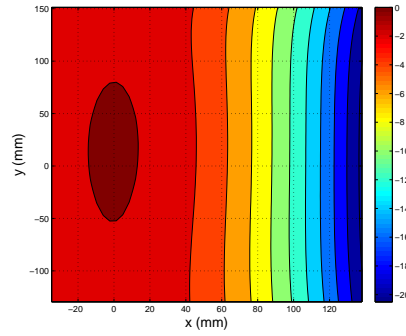

Figure 7: Geometry used for error estimation

Figure 8: Isovalues of vertical height *z* of bistable plate, showing subtle doubly curved regions
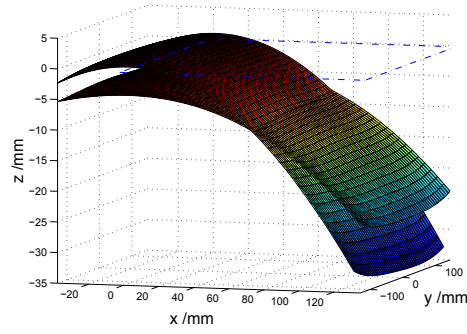

Figure 9: Shapes of bistable plate at 53Hz, at opposite peaks of oscillation. Dashed lines show the approximate plan area of the half plate

The distance h between (x, y) and $(\hat{x}, \hat{y})$ is readily calculated using Pythagoras theorem, and this may be scaled into true dimension units by:

$$H = h\frac{Z}{f} \tag{11}$$

An equivalent metric H' can be calculated in the virtual image system.

These variables were calculated for all points in a sample image, and both H and H' showed a half-normal statistical distribution, with no apparent geometrical bias around the image, suggesting the dominant source of error was random digitisation noise. The 90th percentiles of H and H' were 0.23mm and 0.07mm respectively.
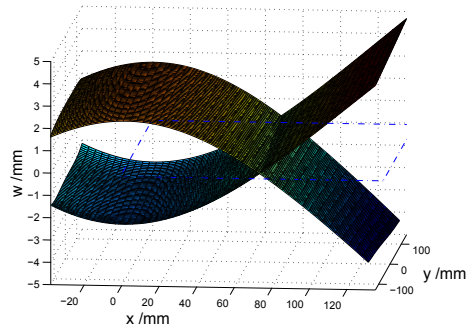
13

Figure 10: Vertical displacements against initial x-y location of bistable plate at 53Hz, at opposite peaks of oscillation. (w represents deflection in the vertical z direction, relative to the original static shape)
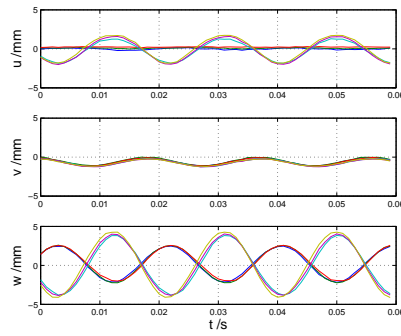

Figure 11: 3D time traces from approximate locations points A-F as shown in Figure 2, showing significant horizontal motion. (u, v and w represent displacement in the horizontal x, y directions and vertical z direction respectively)
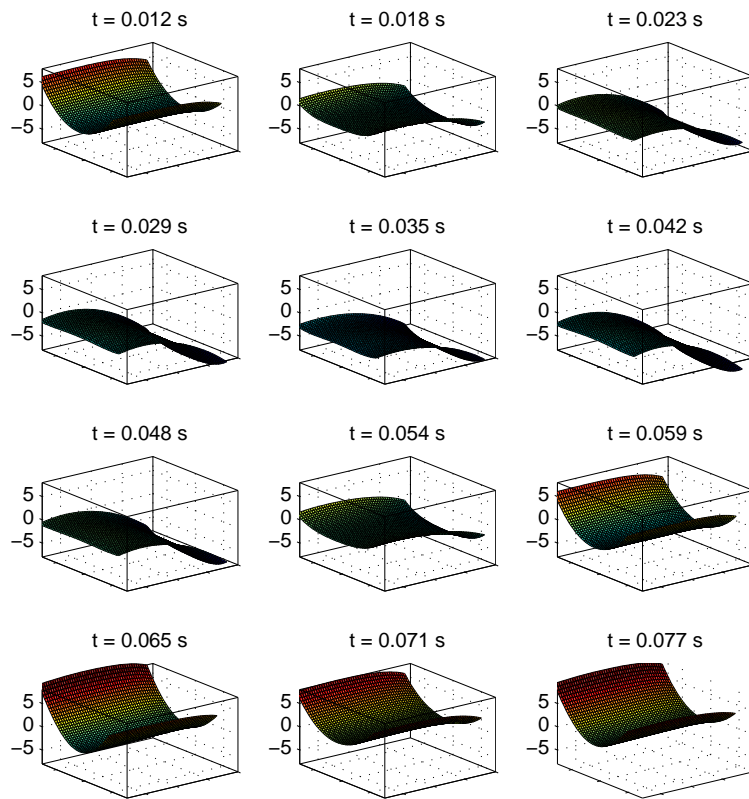
Figure 12: 3D sequence of plate snapping at 40.3Hz excitation. The first 3 frames show the plate snapping between stable states, then frames 4 to 6 show a small oscillation without snapping. Frames 7 to 9 show the plate snapping back, and frames 10 to 12 show another small oscillation before the sequence repeats. Frames 2 and 8 show that the plate forms a saddle configuration when midway through a snapping motion. Note that as in Figures 9 and 10 a little over half the plate is shown in the *x*-direction

5 Results from Case Study

This section presents some results from a case study experiment that highlights the insight that this method can give.

5.1 True Static Shape of Bistable Plate

Figure 8 shows the described method being used to capture the static shapes of the structure under test (as described in Section 2), and is far quicker than the equivalent full field measurements using dial gauges etc. The insight into the variation in curvature across the model can be used to refine and validate analytical models and Finite Element Analysis models.

5.2 Small Amplitude Beam-like Oscillations of Bistable Plate

Figure 9 shows the shapes of the plate at the extremes of a single vibration mode. Figure 10 subtracts the shape of the appropriate static configuration to show the vertical deflection of the same mode. Together these figures demonstrate how clearly the method captures the deflection shape and locates the node lines of the vibration. Figure 11 shows time traces taken at various points on the plate from which it is clear that a displacement in the x direction exists at certain points, along with the more obvious deflection in the vertical z direction.

5.3 Large Snapping Oscillations of Bistable Plate

Figure 12 shows a continuous snapping oscillation of a plate. This is a good test of the proposed technique as the snapping results in a rapid large deflections of the plate. For the first two frames, the plate is 'u' shaped along the y direction; it then 'snaps' into a 'n'shape in the x direction and performs a small oscillation, before snapping back to the 'u' shape and performing another small oscillation before the cycle repeats. Note that the central point of the oscillation is a saddle shape, a shape that is neither one of the plate's stable positions.

6 Conclusions and future work

This paper has shown that a single high speed camera can be adapted with the use of a single mirror to provide full 3D motion capture of the vibration plates which are lightweight, exhibit large amplitude deflections, nonlinear responses and are initially curved. Therefore the method can provide more detailed data than existing methods, which have limitations such as the addition of unwanted mass, problems with configuration, unwanted assumptions about the motion of the plate under test, or lack of quantitative results.

The paper has described the necessary workings for resolving the three-dimensional locations of points, and for an interactive means of calibrating the camera that avoids the need to physically measure many key parameters in the configuration of the method.

Finally the paper has shown some sample results, which demonstrate the clarity of insight that can be achieved, and include detailed images of a bistable plate during snapping motion. Therefore the method described here has been shown to be of use where measurements of complex surface vibrations is required.

It should be noted that once the image has been separated into true and virtual portions, and the necessary reflection transformation has been performed on the virtual image, it is feasible to apply a wide range of stereoscopic imaging strategies for calibration or correspondence, as alternatives to the simple methods described here. In particular, if greater accuracy is desired for smaller amplitude vibrations, it may be desirable to relax the assumption that the 'virtual' camera is identical to the true camera, and use distortion modelling techniques to take account of distortions within both effective camera systems, hence compensating for any distortions due to the mirror. Adapting this method to different test specimens could utilise radically different solutions to the correspondence problem; for example speckle-pattern based methods could be used where it is possible to paint the plate. Such work could lead to invaluable new experimental work in the field of dynamics.

7   acknowledgements

References

[1] A. Carrella, M.I. Friswell, A. Pirrera, and G.S. Aglietti. Numerical and experimental analysis of a square bistable plate. In *International Conference on Noise and Vibration (ISMA 2008)*, 2008.

[2] M. Dano and M. Hyer. Thermally-induced deformation behavior of unsymmetric laminates. *International Journal of Solids and Structures*, 35(17):2101 – 2120, 1998.

[3] S. Daynes, P. Weaver, K. Potter, P. Margaris, and P. Mellor. Bistable composite flap for an airfoil. *Journal of Aircraft*, 47:334–338, 2010.

[4] Cezar G. Diaconu, Paul M. Weaver, and Filippo Mattioni. Concepts for morphing airfoil sections using bi-stable laminated composite structures. *Thin-Walled Structures*, 46(6):689 – 701, 2008.

[5] J. Etches, K. Potter, P. Weaver, and I. Bond. Environmental effects on thermally induced multistability in unsymmetric composite laminates. *Composites Part A: Applied Science and Manufacturing*, 40(8):1240 – 1247, 2009.

[6] D.J. Ewins. *Modal testing: theory, practice, and application*. Mechanical engineering research studies: Engineering dynamics series. Research Studies Press, 2000.

[7] O. Faugeras. *Three-Dimensional Computer Vision, A Geometric Viewpoint*. MIT Press, 1993.

[8] Mathworks Inc. Matlab and simulink for technical computing, 2011.

[9] I-Chen Lin, Jeng-Sheng Yeh, and Ming Ouhyoung. Extracting realistic 3d facial animation parameters from multiview video clips. *IEEE Computer Graphics and Applications*, 22:72–80, 2002.

[10] J. Ma, R. Cole, B. Pellom, W. Ward, and B. Wise. Accurate automatic visible speech synthesis of arbitrary 3d models based on concatenation of diviseme motion capture data. *Computer Animation and Virtual Worlds*, 15:485 500, 2004.

[11] H.W. Schreier M.A. Sutton, J. Orteu. *Image Correlation for Shape, Motion and Deformation Measurements*. Springer, 2009.

[12] Mark Pankow, Brian Justusson, and Anthony M. Waas. Three-dimensional digital image correlation technique using single high-speed camera for measuring large out-of-plane displacements at high framing rates. *Appl. Opt.*, 49(17):3418–3427, Jun 2010.

[13] Torsten Putze, Karsten Raguse, and Hans-Gerd Maas. Configuration of multi mirror systems for single high-speed camera based 3d motion analysis. *Videometrics IX*, 6491(1):64910L, 2007.

[14] Anthony B. Stanbridge, Milena Martarelli, and David J. Ewins. Measuring area vibration mode shapes with a continuous-scan ldv. *Measurement*, 35(2):181 – 189, 2004.

[15] Anthony B. Stanbridge, Milena Martarelli, and David J. Ewins. Single-camera stereovision setup with orientable optical axes. *Computational Imaging and Vision*, 35(2):181 – 189, 2004.